Earth Planet. Sci. Lett. 649 (2025) 119103

Contents lists available at ScienceDirect

Earth and Planetary Science Letters

journal homepage: www.elsevier.com/locate/epsl

Poroelastic effects on rupture propagation across fault stepovers

Luyuan Huang [a,b], Elías Rafn Heimisson [c], Luca Dal Zilio [d,e,*]

[a] Institute of Geophysics, China Earthquake Administration, Beijing, China
[b] Institute of Geophysics, Department of Earth Sciences, ETH Zürich, Switzerland
[c] Institute of Earth Sciences, University of Iceland, Reykjavík, Iceland
[d] Earth Observatory of Singapore, Nanyang Technological University, Singapore, Singapore
[e] Asian School of the Environment, Nanyang Technological University, Singapore, Singapore

ARTICLE INFO

Editor: C. Lithgow-Bertelloni

Keywords:
Poroelasticity
Strike-slip stepover
Earthquake cycle
Rate-and-state friction
Numerical modeling

ABSTRACT

The role of poroelasticity in influencing the frequency of ruptures jumping through strike-slip stepovers remains unclear. To understand how poroelastic effects govern long-term rupture behavior in strike-slip fault systems with stepovers, we conduct earthquake sequence simulations incorporating undrained pore pressure responses across the full spectrum of Skempton's coefficient. Our findings reveal that Skempton's coefficient significantly affects the effective normal stress, which can either cause fault clamping or unclamping, and ultimately influences rupture propagation across fault stepovers. The likelihood of rupture jumping is predominantly determined by Skempton's coefficient and the width of the stepover, with Skempton's coefficient showing an approximately linear relationship to the critical jumpable step size. Specifically, a higher Skempton's coefficient facilitates rupture jumping across fault segments, even over larger stepover distances. Analytical solutions involving dislocation and Skempton's coefficient provide practical methods for evaluating pore pressure changes and associated seismic hazards near fault stepovers. Our statistical analysis identifies a critical jumpable width of 4.4–5.1 km due to static stress transfer, assuming a typical range of Skempton's coefficient for compressional stepovers, beyond which ruptures are unlikely to propagate. This study underscores the potential of using physics-based earthquake sequence models to reflect statistical fault rupture behaviors. Given that multi-segment earthquake ruptures present challenges in assessing maximum rupture lengths, our findings offer crucial insights into the role of poroelastic effects and the conditions that facilitate or limit rupture propagation across fault stepovers.

1. Introduction

Faults are frequently not isolated structures but act as integral components of a broader network of geological fractures that can interplay through stress fields (Scholz and Gupta, 2000) (Fig. 1). Earthquakes that occur in the setting of intricate fault networks are capable of extending across multiple fault segments during major events. For instance, the 2016 Mw 7.8 Kaikōura earthquake, which is considered the most complex rupture event recorded to date, ruptured at least 21 segments of the Marlborough fault system (Ulrich et al., 2019) (Fig. 1a). The rupture behaviors in the context of multiple fault segments are strongly affected by the fault interaction. Recent studies demonstrated complex stress interactions between the 2019 Mw 6.4 and 7.1 Ridgecrest earthquakes, including dynamic and static triggering (Goldberg et al., 2020; Taufiqurrahman et al., 2023). Fault interaction, wherein an earthquake on one fault may alter the tectonic stress conditions of nearby faults — potentially affecting the timing of subsequent seismic events — offers critical insights for seismic source characterization and earthquake hazard assessment (Stein, 1999; Scholz and Gupta, 2000).

Understanding the ability of multiple fault segments to rupture simultaneously within a single earthquake event is crucial for assessing the potential upper limits of earthquake magnitudes, as the seismic moment increases proportionally with the area ruptured. Variations in stress along a rupture and the complex geometries of fault traces are key factors in determining the maximum rupture length (Wesnousky, 2006, 2008). Fault stepovers, characterized by offset, parallel fault segments at the Earth's surface, represent one type of geometric complexity that can influence rupture length. The 1992 Landers earthquake is an ideal instance of such a scenario — it ruptured at least four fault segments ex-

* Corresponding author at: Earth Observatory of Singapore, Nanyang Technological University, Singapore, Singapore.
E-mail address: luca.dalzilio@ntu.edu.sg (L. Dal Zilio).

https://doi.org/10.1016/j.epsl.2024.119103
Received 31 May 2024; Received in revised form 15 October 2024; Accepted 29 October 2024
Available online 19 November 2024

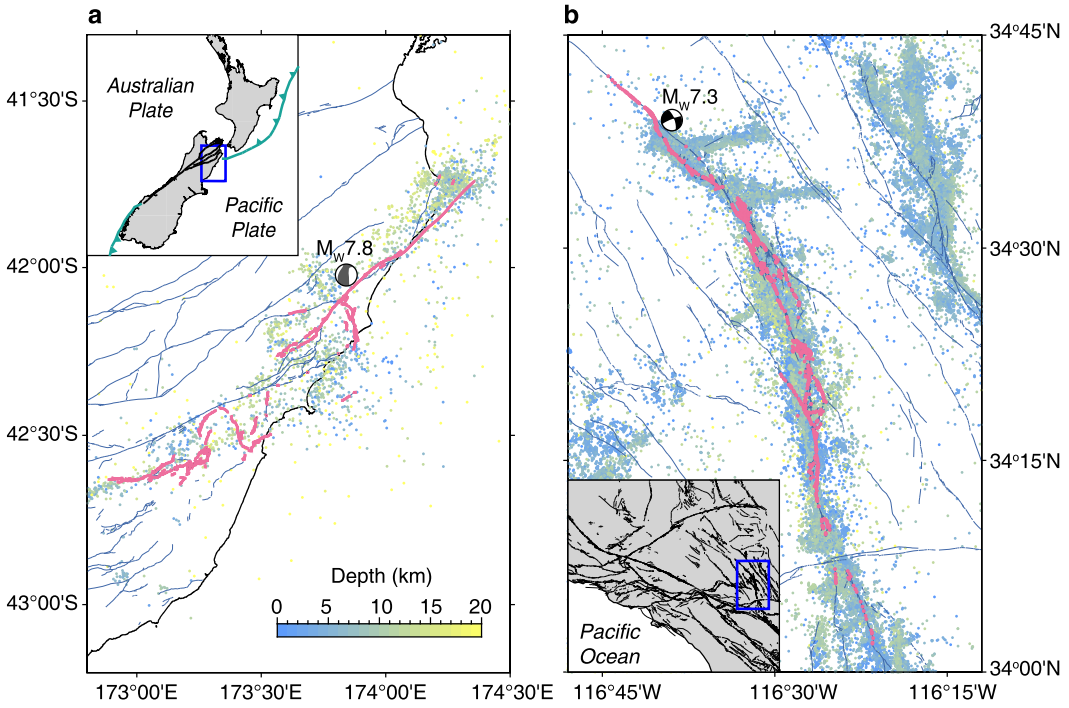

Fig. 1. Rupture traces of (**a**) the 2016 M_W 7.6 Kaikōura earthquake and (**b**) the 1992 M_W 7.3 Landers earthquake. The pink lines in panels (**a**) and (**b**) denoting the surface trace are from the New Zealand Active Faults Database and SURE 2.0 database (Nurminen et al., 2022), respectively. The colored dots in panel (**a**) represent the relocated seismicity following the 2016 M_W 7.6 Kaikōura earthquake (Lanza et al., 2019). The colored dots in panel (**b**) indicate the relocated earthquakes between 1992 and 2022 provided by the Southern California Earthquake Data Center (SCEDC). Black and gray beach balls indicate the focal mechanism solutions of the 1992 M_W 7.3 Landers earthquake and the 2016 M_W 7.6 Kaikōura earthquake, respectively. The color bar represents the depths of the seismicity.

hibiting a right-stepping pattern to the north and generated a Mw 7.3 event (Sieh et al., 1993) (Fig. 1b).

Ample numerical (e.g., Segall and Pollard, 1980; Harris and Day, 1993; Duan and Oglesby, 2006) and observational studies (e.g., Wesnousky, 1988; Sieh et al., 1993; Wesnousky, 2006) revealed that ruptures propagating within a stepover system can be arrested by greater stepover widths — that is, the amount of horizontal offset between the discrete fault segments. Field observations found that seismic ruptures could not propagate across compressional stepovers with step widths exceeding 5 km or extensional stepovers featuring step widths over 8 km (Wesnousky, 1988; Knuepfer, 1989). Dynamic modeling of earthquake sequences and aseismic slip establishes a physics-based framework for predicting seismic behavior in fault stepovers, highlighting that factors like poroelasticity, off-fault plasticity, friction laws, seismogenic depth, and background stress significantly influence rupture jumping and seismic complexity (e.g., Harris and Day, 1993; Bai and Ampuero, 2017; Kroll et al., 2023; Mia et al., 2024). Particularly, including pore pressure effects has been shown to modify the critical stepover distance, a key factor determining whether seismic ruptures can propagate across fault segments (Sibson, 1985; Harris and Day, 1993; Jónsson et al., 2003).

Numerous faults at seismogenic depths can be depicted as fractures embedded in a fluid-infiltrated porous rock, and thus, the poroelastic response to frictional sliding is crucial for rupture propagation. The role of poroelastic effects in fault frictional slip has drawn continued attention for decades (e.g., Dunham and Rice, 2008; Heimisson et al., 2019, 2022; Rice and Cleary, 1976; Rice and Simons, 1976; Rudnicki and Koutsibelas, 1991; Rudnicki and Rice, 2006; Zhu et al., 2020; Dal Zilio et al., 2022; Dal Zilio and Gerya, 2022). In-plane slipping along the fault leads to compaction on one side and dilatation on the other. As a result, there is an instantaneous response in slip-driven pore pressure, which exhibits opposite signs on each side of the fault. Consequently, the positive slip-driven pore pressure change in the overlap area of the compressional stepover produces unclamping effects, while the negative pore pressure change in the overlap area of the dilatational stepover generates clamping effects. Sibson (1985) proposed that extensional steps could act to halt the propagation of seismic ruptures. This theory posits that decreased stress at a dilatational stepover swiftly opens extension fractures, with insufficient time for fluid pressure therein to re-equilibrate during rupture propagation. Therefore, this sudden rise in effective normal stress increases frictional strength, arresting earthquake rupture.

The investigation into how poroelasticity influences the likelihood of an earthquake jumping through a stepover emerges as a significant area of study. Dynamic rupture simulations (Harris and Day, 1993; Liu and Duan, 2014) have incorporated undrained pore pressure changes to explore the impact of poroelasticity on the critical stepover width. Liu and Duan (2014) proposed the critical width for compressive stepovers from 3500 m to 4500 m and, conversely, reduced it from 5000 m to 1000 m for dilatational stepovers. However, these studies commonly utilize a standard Skempton's coefficient B of 0.8, a value that may not be fully supported by comprehensive observational data (e.g., Cheng, 2016). Additionally, while single dynamic rupture simulations investigate the effects of poroelasticity, they often require the artificial introduction of initial stresses, potentially misaligning with the spatially heterogeneous stress conditions observed across multiple earthquake cycles. It is also important to recognize that simulations focused on individual events do not provide information about the frequency at which ruptures propagate across stepovers. In contrast, earthquake sequence simulations, despite their initial assumptions, progressively diminish the impact of these assumptions over multiple seismic cycles, offering insights into the frequency of rupture propagation across stepovers.

We expand on previous work by performing earthquake cycle simulations adopting a quasi-dynamic boundary element code developed by Heimisson (2020). We further incorporate undrained pore pressure responses affecting the fault's clamping and unclamping effects, and the boundary element model is governed by rate-and-state friction, with state evolution determined by the aging law. We first depict the physical process of rupture propagation across a compressional stepover embedded in a poroelastic medium. We then conduct a thorough pa-

rameter space study, evaluating the effects of Skempton's coefficient variations and stepover width on the likelihood of ruptures jumping across the stepover within a fluid-filled porous environment. In the next phase, we validate this model against an analytical solution involving a plane strain shear dislocation on a leaky plane within a linear poroelastic, fluid-saturated solid. This validation serves two purposes: first, to demonstrate the robustness of the numerical model, and second, to showcase the potential of predicting pore pressure changes induced by fault slip in a straightforward and efficient manner using the analytical solution. Lastly, we use the physics-based earthquake sequence model to derive a statistically critical jumpable stepover width, over which the rupture has an equal chance to pass through or terminate.

2. Methods

2.1. Boundary element methodology

In our earthquake sequence simulations, the shear stress change and normal stress change are expressed as the integral of the kernel function multiplied by the fault slip. By discretizing the fault into N elements, the shear and normal stress variations on the i-th element can be represented as:

$$\Delta\tau_i = \sum_j^N G_{ij}^{\tau}\delta_j, \tag{1}$$

$$\Delta\sigma_i = \sum_i^N G_{ij}^{\sigma}\delta_j. \tag{2}$$

Where, G_{ij}^{τ} and G_{ij}^{σ} are dense stiffness matrices for the shear stress and normal stress, respectively, which are calculated using the analytical solutions for elastic dislocations in full-space (Nikkhoo et al., 2016). δ_j is the relative slip vector on the j-th element. The fault is loaded by steady sliding from adjacent creeping zones (the extension of the fault) (e.g., Ozawa et al., 2023) instead of using a backslip approach (e.g., Richards-Dinger and Dieterich, 2012; Heimisson, 2020; Yin et al., 2023) to prevent unphysical stress accumulation. The behavior of the frictional interface is governed by rate- and state-dependent friction laws and the aging law (Dieterich, 1979, 1981; Ruina, 1983; Marone, 1998; Beeler et al., 1996, 2008):

$$\tau = (\sigma - p)\left[f_0 + a\,ln\left(\frac{V}{V_0}\right) + b\,ln\left(\frac{V_0\,\theta}{D_{RS}}\right)\right], \tag{3}$$

$$\dot{\theta} = 1 - \frac{V\theta}{D_{RS}}, \tag{4}$$

$$\tau = \tau_0 + \Delta\tau - \eta V, \tag{5}$$

$$\sigma = \sigma_0 + \Delta\sigma, \tag{6}$$

$$\eta = \frac{\mu}{2\,C_s}. \tag{7}$$

Where, V is the slip rate, V_0 is the reference sliding velocity, θ is the state variable, f_0 is the reference friction coefficient, a is the coefficient of the direct effect, b is the coefficient of the evolution effect, and D_{RS} is the characteristic slip distance. τ_0 and σ_0 are initial shear and normal stress, respectively. μ is the shear modulus, and C_s represents the shear wave speed. Eq. (7) represents the radiation damping term, an approximation of inertia (Rice, 1993). Earthquake sequence simulations employing this approximation are referred to as "quasi-dynamic". The impact of this approximation has been investigated in prior research (Lapusta and Liu, 2009; Thomas et al., 2014).

2.2. Undrained pore pressure effect

The term "undrained" denotes the absence of any fluid migration during the short duration of the earthquake rupture. The effective normal stress ($\overline{\sigma} = \sigma - p$) in Eq. (3) combines the static normal stress σ with the dynamic pore pressure changes p. As defined by Rice and Cleary (1976), the pore pressure p is given by:

$$p = B \times \frac{\Delta\sigma_{kk}}{3}, \tag{8}$$

where B is Skempton's coefficient and $\Delta\sigma_{kk}/3$ represents the average stress change. Note that in Eq. (8), compression is considered positive, which is opposite to the sign convention used by Rice and Cleary (1976). The undrained pore pressure change in the i-th element can be expressed as:

$$p_i = \sum_j^N \frac{B}{3} G_{ij}^{\sigma_{kk}}\delta_j, \tag{9}$$

where $G_{ij}^{\sigma_{kk}}$ is the dense stiffness matrix for the sum of the principal stress variation, which is derived by the analytical solutions for elastic dislocations in full-space (Nikkhoo et al., 2016). δ_j is the relative slip vector on the j-th element.

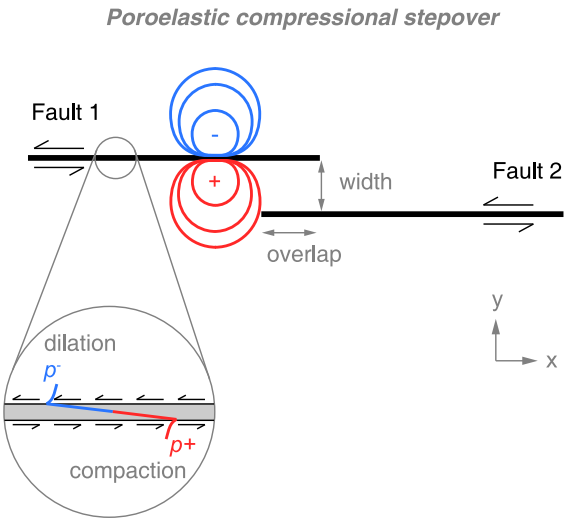

Fig. 2. Model setup. Colored lines and lobes indicate the pore pressure change induced by the fault slip. The red and blue colors represent the positive and negative pore pressure changes, respectively.

2.3. Model setup

We design a 2D domain under plane strain conditions, embedding two left-lateral strike-slip fault segments, each 36.5 km in length, within a homogeneous medium (Fig. 2). These segments overlap by 5 km, forming a compressional stepover. To explore how the poroelastic effects influence the rupture propagation across the stepover, both stepover width and Skempton's coefficient are variable in our simulation (Fig. 2). Both fault segments are characterized as velocity-weakening zones, with parameters set to $a = 0.01$ and $b = 0.0125$. The initial normal stress σ_0 is 50 MPa, and the initial shear stress $\tau_0 = f_0\,\sigma_0 + \eta\,V_0 \approx 30$ MPa. The initial state $\theta_0 = D_{RS}/V_0\,(1+\psi(0, 0.01))$, where $\psi(m, s)$ represents Gaussian noise with mean value m and standard deviation s.

For earthquake sequence simulations, achieving a stringent numerical model resolution is essential, as it ensures the accurate resolution of both rupture nucleation and propagation processes. Specifically, it is essential to rigorously examine two physical length scales to address these complexities effectively. The first physical length, well known as the width of the cohesive zone or process zone (L_b), is suggested to be 3 to 5 times larger than the grid size Δx within boundary integral models (Day et al., 2005) and can be expressed as follows:

$$L_b = \frac{\mu\,D_{RS}}{b\,\sigma}. \tag{10}$$

Table 1
Parameter values and model geometries.

Symbol	Description	Value
Material properties		
υ_u	Undrained Poisson's ratio	0.35
μ	Shear modulus	30 GPa
C_s	Shear wave speed	3.5 km/s
Frictional Properties		
D_{RS}	Characteristic slip distance	5000 μm
a	RSF direct effect	0.01
b	RSF evolution effect	0.0125
V_0	Reference sliding velocity	10^{-9} m/s
f_0	Reference friction coefficient	0.6
σ_0	Initial normal stress	50 MPa
Fault Geometry		
L_f	Fault segment length	36.5 km
O	Overlapped length	5 km
Δx	Grid size	61 m
Other parameters dependent on parameters above		
η	Radiation damping	$\mu/(2C_s) \approx 4.3$ MPa · s/m
τ_0	Initial shear stress	$f_0\sigma_0 + \eta V_0 \approx 30$ MPa
θ_0	Initial state	$D_{RS}/V_0(1 + \psi(0, 0.01))$
L_b	the cohesive zone length	366 m
L_∞	the nucleation size	2938 m
Notes		
$\psi(m, s)$	Gaussian noise, mean m, std. s	

Heimisson (2020) found that the 2-D earthquake sequence simulation can be resolved in the case of $L_b/\Delta x$ as low as 1.5 using the algorithm described in his study, whereas Jiang et al. (2022) resolved L_b with at least 4 elements at their benchmark exercises. Yin et al. (2023) proposed that the stable nucleation can be captured with $L_b/\Delta x$ as low as 2.2 in their 3-D simulations. Through a convergence test (see Fig. S1 in the supplementary material), we keep $L_b/\Delta x$ equals 6 in our simulations to assure the cohesive zone is well resolved.

The second length scale determines the minimum half-length of the unstable zone over which spontaneous nucleation may emerge, which can be quantified as follows (Rubin and Ampuero, 2005):

$$L_\infty = \frac{\mu\, b\, D_{RS}}{\pi\, \sigma (b-a)^2}. \tag{11}$$

Extensive research studies have consistently demonstrated that seismic sequence complexity, characterized by both full and partial ruptures, tends to occur when the width of the velocity weakening zone (W) sufficiently surpasses L_∞ (e.g., Barbot, 2019; Cattania, 2019; Heimisson, 2020). In anti-plane earthquake sequence simulations conducted by Cattania (2019), a systematic exploration of the parameter space reveals that when the ratio W/L_∞ exceeds 10, partial rupture emerges. To ensure robust catalog statistics in our study, it is crucial to obtain a sufficient number of events during an extended simulated period that encompasses multiple full cycles, interspersed with smaller events. The adoption of a variable time-stepping approach allows us to effectively strike a balance between achieving a suitable W/L_∞ ratio, ensuring well-resolved L_b, and maintaining a realistic simulation time. The model parameters used in this study are listed in Table 1.

3. Results

3.1. Rupture dynamics and stress interaction in poroelastic stepovers

The effective normal stress within a compressional stepover is modulated by the interplay between two key factors: (1) the normal stress driven by compaction within the rock matrix, and (2) the pore pressure changes regulated by Skempton's coefficient alongside average stress variations. Consequently, it is evident that Skempton's coefficient has the potential to impact the effective normal stress, which determines whether the fault is clamping or unclamping.

As depicted in Fig. 3, the propagation of rupture induces stress changes, consequently causing variations in average stress that lead to time-dependent undrained pore pressure changes. In the scenario where the rupture approaches the tip of Fault 1 (i.e., snapshot at t3 in Fig. 3), both the normal stress and average stress are increasing; thus, whether the undrained pore pressure change sufficiently reduces the effective normal stress depends on Skempton's coefficient. A high Skempton's coefficient (e.g., $B = 0.8$) has the capability of generating sufficient dynamic pore pressure change, hence making the overlapped area on the second fault, i.e., Fault 2, unclamped (Fig. 3b), which facilitates the rupture propagating across the stepover. In contrast, a lower Skempton's coefficient (e.g., $B = 0.2$) results in a lower pore pressure change, which may be insufficient and therefore cause the tip of Fault 2 near the overlap zone to be clamped (Fig. S2).

Since fault slip behavior is not solely determined by effective normal stress, we also included the temporal evolution of Coulomb failure stress to monitor changes in fault stability conditions under both high and low Skempton's coefficient scenarios with the same stepover width (Fig. S3). In the case of a low Skempton's coefficient (e.g., $B = 0.2$), as rupture propagates on Fault 1 towards the overlapping region, a Coulomb stress shadow forms at the left tip of Fault 2. This leads to the arrest of the rupture, while the following event initiates in the right half segment of Fault 2, where the Coulomb stress is positive. Stress shadows emerge in lobes surrounding the rupture tips, which frequently mitigate or eradicate seismicity on nearby faults within their scopes (e.g., Harris and Simpson, 1998). In contrast, when rupture propagates on Fault 1 with a high Skempton's coefficient (e.g., $B = 0.8$), it is easier to generate positive Coulomb stress at the left tip of Fault 2. As a result, the rupture is more likely to jump across the stepover. In the scenario of an extensional (dilatational) stepover, the reduction of pore pressure near the overlap area induces clamping effects on the receiver fault, making it easier for the rupture to be arrested (Fig. S4).

It is worth noting that in the case of a single event, numerical simulations can only determine a binary outcome for rupture propagation across the stepover — either jumping or arresting, as shown in Fig. 3 and Fig. S2. Expanding the analysis from a single event to multiple earthquake cycles reveals variations in the frequency of rupture propagation across the stepover, across the full range of Skempton's coefficient (from 0 to 1). These variations are due to differences in the spatiotemporal evolution of effective normal stress, which are influenced by distinct undrained poroelastic effects driven by Skempton's coefficient.

3.2. Fault slip and poroelastic influences over multiple seismic cycle

Our earthquake sequence simulations are capable of modeling multiple earthquake cycles, which can potentially alter the stress field and consequently affect long-term fault interactions. In order to examine how poroelasticity influences long-term fault slip behavior, we utilized two distinct end-member models with different Skempton's coefficients to generate extended sequences of fault slip evolution, as depicted in Fig. 4.

These two end-member models depict diverse degrees of fault interactions. In the model that does not consider poroelastic effects, only a subset of the earthquakes are triggered by the activity on the neighboring fault (Fig. 4a). The mechanical interactions between the two faults result in an aperiodic sequence of full and partial ruptures punctuated by occasional slow-slip events (Figs. 4a and 4c). Previous studies have indicated that the rupture styles, derived from earthquake cycle simulation, in which a single velocity-weakening asperity is embedded within a velocity-strengthening domain, are primarily controlled by the ratio of the size of the velocity-weakening (VW) region to the nucleation length (Cattania, 2019; Barbot, 2019). Moreover, Barbot (2021) proposed that this ratio has a strong control on the degree of mechanical interactions among parallel faults. As this ratio increases — effectively reducing the

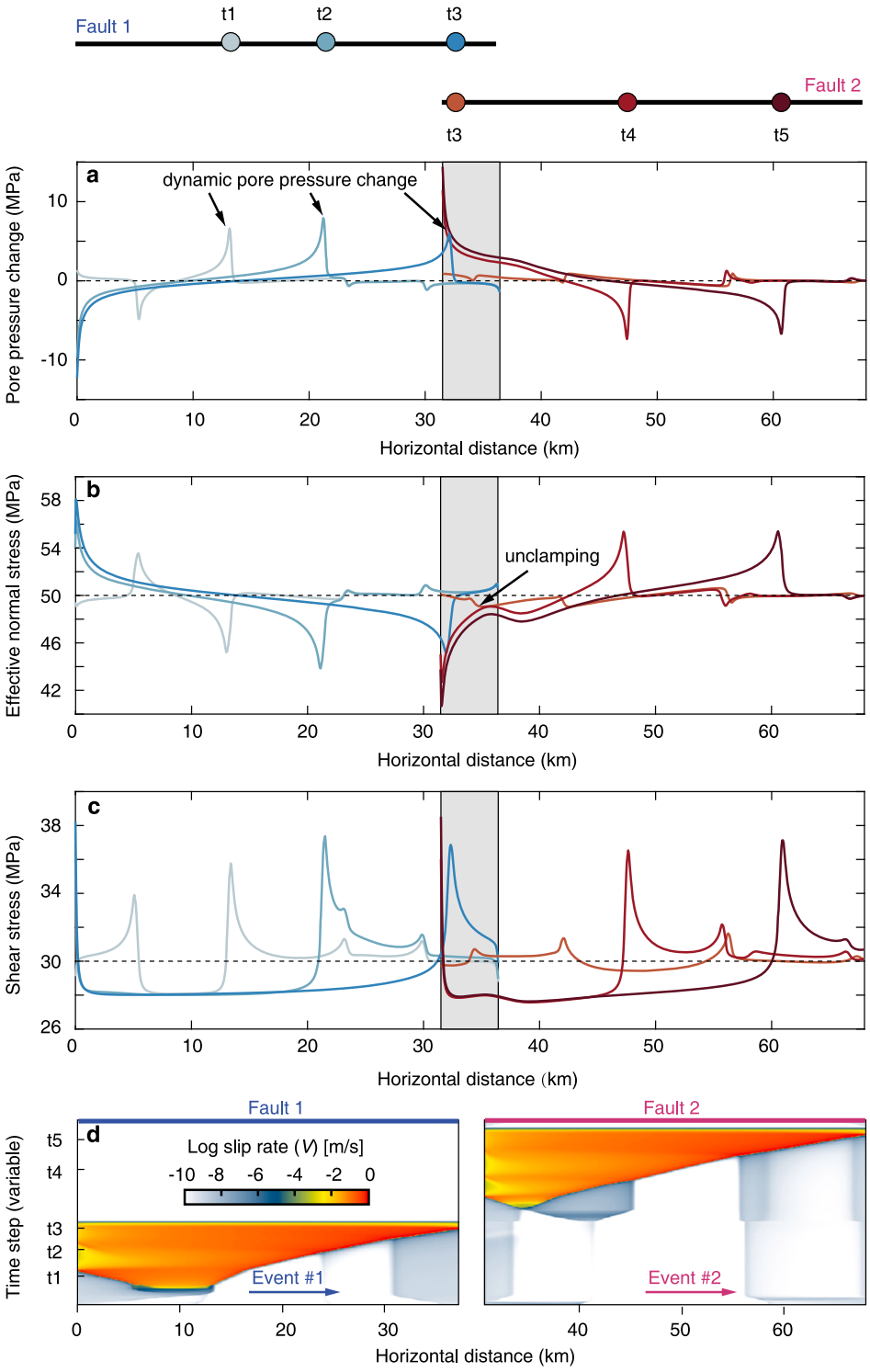

Fig. 3. Temporal evolution of (**a**) pore pressure changes, (**b**) effective normal stress, (**c**) shear stress, and (**d**) slip rate when the rupture propagates within a compressional stepover. Skempton's coefficient is 0.8, and the stepover width is 3.6 km. The colored lines in panels (**a**)–(**c**) represent different time steps, corresponding to t1–t5 shown in panel (**d**).

characteristic nucleation length — the faults become more unstable. Consequently, fault interactions within the network become stronger, ultimately leading to tight synchronization of seismicity. In our simulation, we also observed an alternative mechanism for influencing fault interactions. When the model had a high Skempton's coefficient (B = 1), it exhibited significantly stronger mechanical interactions within the stepover system. This synchronization is evident as it results in nearly simultaneous earthquakes on two faults (Fig. 4b). These simulations demonstrate that an increase in Skempton's coefficient corresponds to a transient reduction of the effective normal stress in the context of a compressional stepover system, destabilizing the fault and increasing the likelihood of dynamic triggering.

Our modeling demonstrates that beyond the frictional properties previously documented (Barbot, 2021), poroelastic effects substantially influence fault interactions, potentially affecting the likelihood of rupture propagation across stepovers. These simulations not only consider

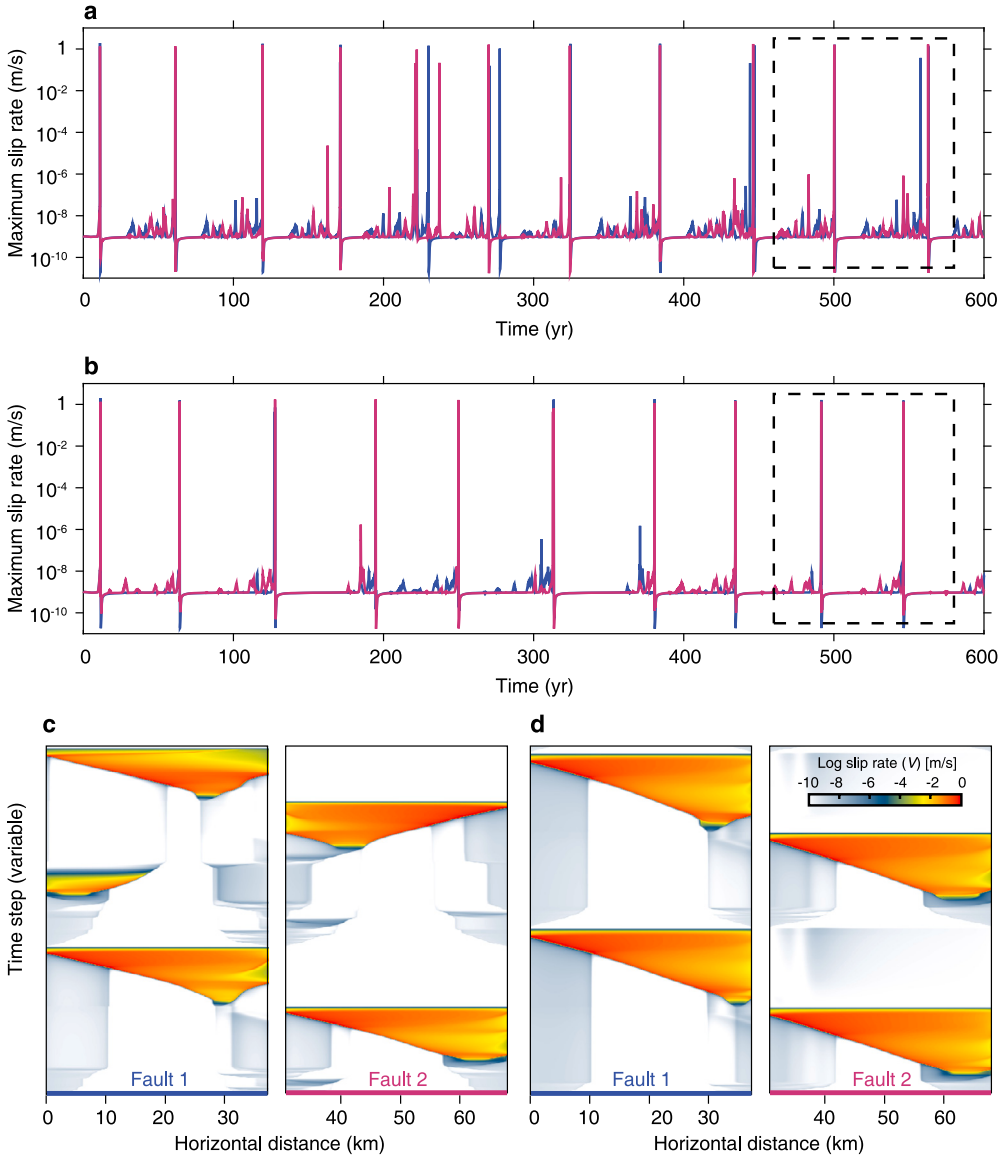

Fig. 4. Long sequence of fault slip evolution for two end-member models. (**a**) Peak slip velocity for faults with $B = 0$. (**b**) Peak slip velocity for faults with $B = 1$. (**c**) Slip evolution within the time window (black dashed box) shown in panel (**a**). (**d**) Slip evolution within the time window (black dashed box) shown in panel (**b**).

the well-studied impact of stepover width (e.g., Segall and Pollard, 1980; Harris and Day, 1993; Duan and Oglesby, 2006; Wesnousky, 1988; Sieh et al., 1993; Wesnousky, 2006), but also highlight the significant role of undrained poroelasticity in facilitating or hindering rupture dynamics.

3.3. Probability of rupture jumping

As shown in Fig. 4, rupture events across the stepover do not consistently result in jumping or termination when simulating a long sequence of earthquakes. Instead, their occurrence follows a certain frequency, reflecting the self-consistent evolution of stress over multiple seismic cycles. To better understand how poroelasticity influences this pattern, we conducted a statistical analysis using our synthetic earthquake catalog. We quantified the probability of rupture jumping, expressed as $C = N_j/(N_j + N_a)$, where N_j represents the count of jumping ruptures and N_a is the count of arresting ruptures.

Distinguishing between jumping and arresting ruptures in our quasi-dynamic simulations requires assuming a timescale due to fault interactions being possible slower than in fully dynamic simulations. For example, with a stepover width of 2 km, the propagation time from the first fault to the second fault in our simulation is on the order of 10^5 seconds (27.7 hours). This propagation time aligns with other quasi-dynamic simulations, such as those by Ozawa et al. (2023), where rupture propagation through fault bends shows inter-event times larger than 10^4 seconds. While the quasi-dynamic approach may not fully capture the rapid dynamic stress perturbations associated with seismic waves — potentially influencing the instantaneous rupture velocity and propagation dynamics — our study focuses on statistically assessing fault interaction patterns and rupture probabilities over multiple earthquake cycles. Unlike fully dynamic models, which often examine single-event rupture jumps (Harris and Day, 1993; Duan and Oglesby, 2006), our objective is to quantify the probability of a source fault triggering a secondary fault within a defined period of up to 3×10^5 seconds. Within this interval, we classify ruptures as either jumping or arresting based on cumulative stress interactions over time: if the second fault activates within this threshold, we classify it as a jumping rupture, indicative of short-delay triggering consistent with a dynamic response. Alternatively, activations occurring beyond this threshold are considered arresting ruptures, reflecting static triggering from redistributed permanent stress. This temporal threshold represents the upper boundary for time required for rupture propagation across the stepover, as observed in our statistical analysis (see Fig. S5), and aligns with findings from a recent study (Mia

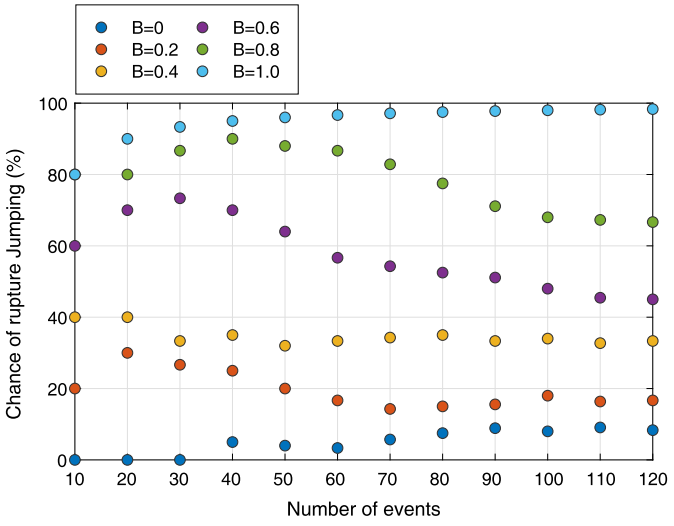

Fig. 5. Percentage of rupture jumping as a function of the number of events. The stepover width here is 4.8 km. The colors represent different Skempton's coefficients.

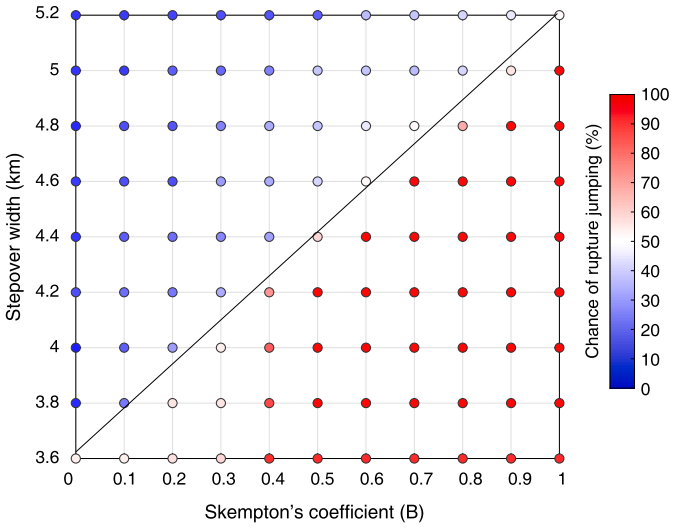

Fig. 6. Percentage of rupture jumping variations depending on both Skempton's coefficient and stepover width. Each data point is computed based on 120 seismic cycles.

et al., 2024) suggesting that delay times on the order of 10^4 to 10^5 seconds capture short-delay interactions within fault clusters. Moreover, recent research (e.g., Im and Avouac, 2024) has demonstrated that slip distributions resulting from rupture propagation across stepover zones can be effectively replicated using a quasi-dynamic method, supporting the suitability of this approach for analyzing rupture triggering over extended timescales.

We acknowledge that the initial conditions in our simulations can influence the likelihood of rupture propagation. However, we chose not to exclude the initial earthquake cycles from our analysis, as is commonly done to minimize initial condition biases (e.g., Romanet et al., 2018). Instead, we analyzed many seismic cycles to observe how the probability of rupture jumping evolved over time (Fig. 5). This approach allowed us to establish a stable estimation of rupture jump probabilities after observing more than 100 seismic cycles. Consistent with findings from previous simulation-based statistical studies (Heimisson, 2020; Yin et al., 2023), a robust statistical assessment typically requires a catalog of over 100 events. Furthermore, we found that a model with a higher Skempton's coefficient for the same stepover width increases the frequency of rupture jumping.

Our parameter study further examined the interplay between Skempton's coefficient and stepover width in influencing the likelihood of rupture jumping. The relationship involves a trade-off: a higher Skempton's coefficient increases the probability of rupture jumping, while a greater stepover width tends to reduce it (Fig. 6). To quantify the critical conditions under which a rupture can propagate across a stepover of a specific width, we focused on identifying the critical stepover width that allows for a 50% chance of rupture jumping. Our analysis revealed an approximately linear relationship between the Skempton's coefficient and the critical jumpable stepover width. In practical terms, this means that a higher Skempton's coefficient correlates with a larger critical jumpable width for the compressional stepover, allowing us to predict the critical width based on the Skempton's coefficient.

4. Discussion

4.1. Comparison with previous studies

Exploring the conditions that influence rupture behavior across stepovers — whether a rupture stops or propagates — remains a central focus in fault dynamics research (e.g., Harris and Day, 1993; Duan and Oglesby, 2006; Liu and Duan, 2014; Ryan and Oglesby, 2014). Our study distinguishes itself through three primary innovations compared to prior work. First, unlike traditional models that apply the slip-weakening friction law lacking a healing mechanism (Ida, 1972), our simulations employ the rate-and-state friction law, which incorporates behaviors such as stick-slip sliding, creep, and healing (Dieterich, 1978, 1979). This approach provides a more realistic representation of multiple seismic cycles. Second, whereas previous studies primarily focused on single-event dynamics (e.g., Harris and Day, 1993; Liu and Duan, 2014; Ryan and Oglesby, 2014), our work extends to probabilistic analyses over multiple seismic cycles, enhancing the understanding of stress evolution and its implications on rupture dynamics. Third, our models incorporate poroelastic effects, addressing the dynamic interaction between subsurface fluids and rock deformation — an aspect crucial to understanding fault dynamics yet often overlooked in conventional dynamic rupture models.

Our simulations also demonstrate the capability of the rate-and-state friction model combined with an evolving stress field over multiple seismic cycles to capture slow-slip transients (Fig. 4). These transients are crucial for understanding the complete spectrum of fault slip behaviors (Peng and Gomberg, 2010). This aspect significantly extends the utility of our modeling approach, providing insights into phenomena that have been observed in natural fault systems but are often omitted in simpler models.

Earlier two-dimensional dynamic rupture models have investigated the effects of fault steps and jumpable stepover widths (e.g., Harris and Day, 1993; Liu and Duan, 2014; Duan and Oglesby, 2006; Finzi and Langer, 2012). These studies provide a benchmark for comparing our findings (see Fig. 7). For instance, Finzi and Langer (2012) studied the influence of Skempton's coefficient on the effective coefficient of friction, $f' = f_0(1 - B)$, under different scenarios. Unlike these studies that mainly focused on extensional stepovers, our research uniquely addresses compressional stepovers and incorporates poroelastic effects, allowing us to explore how dynamic normal stress changes influence rupture propagation.

We begin our analysis by revisiting Harris and Day (1993), who identified a maximum jumpable stepover width of 2.5 km for compressional stepovers without poroelastic considerations. This finding is consistent with Duan and Oglesby (2006), who observed that ruptures in their simulations failed to cross stepovers wider than 2 km during initial events (see Fig. 7). Our results confirm this limitation, with our first seismic event failing at a 2-km-wide compressional stepover. However, subsequent events in our simulations suggest that evolving stress distributions can facilitate the crossing of wider stepovers, achieving

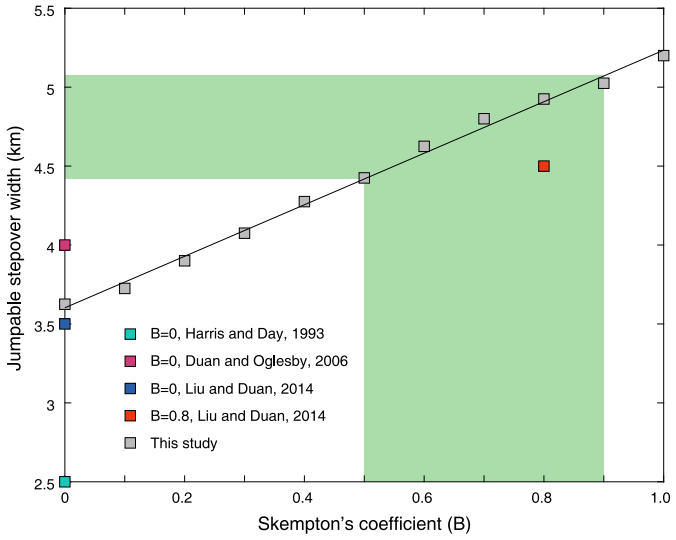

Fig. 7. Comparison with previous studies. The jumpable stepover widths are derived from our simulation-based statistical analysis, representing the equal frequency of rupture jumping and termination. The green shadow indicates the critical jumpable stepover width corresponding to the typical Skempton's coefficient range of 0.5–0.9.

a critical jumpable width of 3.6 km. This is slightly less than the 4 km maximum reported by Duan and Oglesby (2006), likely due to our quasi-dynamic approach that excludes wave-mediated stress transfers. Moreover, aligning with the findings of Liu and Duan (2014), which indicated jumpable stepover distances under 'dry' and 'wet' conditions with Skempton's coefficients of 0 and 0.8, respectively, our simulations demonstrate comparable widths of 3.6 km in 'dry' conditions and 4.9 km in 'wet' conditions. The probabilistic nature of our simulations, assuming a 50% likelihood of rupture propagation, suggests these are upper limits for feasible fault distances. Although our study does not fully account for inertial wave-mediated effects during seismic ruptures, it provides a valuable qualitative assessment of rupture propagation mechanisms, aligning with recent quasi-dynamic studies such as those by Ozawa et al. (2023), which discuss rupture arrest mechanisms at fault bends using Griffith's energy balance theory.

It is worthy noting that the rupture behaviors at stepovers in simulations with the rate- and state-dependent friction law and the slip-weakening friction law may be different (Kroll et al., 2023). On slip-weakening friction faults, rupture jumping happens immediately when positive stress changes push a sufficiently large patch of the receiver fault past its yield stress. In contrast, on rate-and-state friction faults, the nucleation process is time- and stress-dependent; therefore, the renucleation on the receiver fault can occur immediately or may be delayed, depending on the coseismic stress change on the source fault. If the stress change is sufficient to trigger rupture, renucleation on the receiver fault occurs immediately; if it raises the stress above steady-state but is not strong enough for immediate renucleation, the process is delayed. Moreover, the integration of bulk plasticity, specifically poroelastoplasticity, may further influence the observed seismicity patterns and jumping frequency (Mia et al., 2024). A previous study (Liu and Duan, 2014) has shown that incorporating bulk plasticity can decrease the maximum jumpable width of a compressional stepover when compared to the poroelastic model. Another mechanism that was not accounted for in this study is dynamic weakening. Rapid shear heating can cause thermal expansion of pore fluids (Rice, 2006; Noda and Lapusta, 2010), and if the surrounding rock in the fault shear zone has sufficiently low permeability, this may reduce effective normal stress and facilitate rupture jumping.

4.2. Potential for predicting the static pore pressure change

We validate our numerical model against an analytical solution involving a plane strain shear dislocation located on the $x < 0$ axis that represents a leaky plane within a linear poroelastic, fluid-saturated solid (Song and Rudnicki, 2017). Since we disregard pore fluid diffusion, the static term of the pore pressure change, which is caused by the suddenly applied dislocation on the negative x axis, can be expressed as follows:

$$\Delta p = -\frac{D\,B\,\mu(1+\nu_u)}{3\pi\,(1-\nu_u)}\,\frac{y}{x^2+y^2}, \tag{12}$$

where D represents the slip of the dislocation, μ is the shear modulus, and ν_u is the undrained Poisson's ratio. x and y represent the coordinates of where the pressure change is evaluated.

Fig. 8 illustrates the comparison between the numerical and analytical solutions for different Skempton's coefficients with the same slip $D = 0.13$ cm. This validation demonstrates the capability of our numerical model to quantitatively predict the static pore pressure change due to the undrained response of the medium during earthquake ruptures. Compared to the analytical solution, which only accounts for the poroelastic response arising from a homogeneous slip on a single fault (Song and Rudnicki, 2017), numerical models have the capability to address geometry complexities and the evolving stress field over multiple earthquake cycles (e.g., Romanet et al., 2018; Barbot, 2021; Ozawa et al., 2023).

On the other hand, the semi-analytical solution proposed by Song and Rudnicki (2017) accounts for pore fluid diffusion, which is not included in our simulation. Even when the diffusion term is ignored, the analytical solution has the advantage of effectively predicting static pore pressure changes. This prediction, which is guided by the static term shown in Eq. (12), primarily depends on fault slip and Skempton's coefficient, offering a straightforward and efficient approach. Coseismic fault slip can be estimated using empirical methods (e.g., Wells and Coppersmith, 1994), and Skempton's coefficient usually varies within a limited range, such as 0.5–0.9 (Rice and Cleary, 1976; Hart and Wang, 1995). As a result, the static pore pressure change caused by the shear dislocation can be reasonably estimated. Currently, in most practical fault stability analyses, pore pressure is typically assumed to be fixed, along with stress measurements, to evaluate the potential for fault slip. For instance, Jaeger et al. (2009) proposed that the ratio of the maximum to minimum effective principle stress, which corresponds to the situation where a critically oriented cohesionless fault is at the frictional limit, is given by:

$$\frac{S_1 - p}{S_3 - p} = [\sqrt{(f^2+1)} + f]^2, \tag{13}$$

here, S_1 and S_3 represent the maximum and minimum principle stress, respectively, while f denotes the static friction on a pre-existing fault. When a fault is located within a network of stepovers, the oscillation of pore pressure changes — induced by nearby fault slip and derived from Eq. (12) — can be integrated into Eq. (13) along with the background pore pressure. This integration provides a comprehensive assessment of fault stability. Such an approach not only enhances the prediction of rupture propagation potential but also determines whether a seismic event might turn into a larger, more catastrophic event. Consequently, this method can improve seismic hazard assessments.

4.3. Implications for seismic hazard

Biasi and Wesnousky (2016) compiled surface rupture traces from 76 past earthquakes worldwide, offering valuable insights into the correlation between discontinuities of the fault traces and the extent of earthquake ruptures. We utilized this comprehensive database, which includes earthquakes up until 2014, and supplemented it with data points from recent seismic events such as the 2019 Ridgecrest earthquake (Goldberg et al., 2020; Ponti et al., 2020) and the 2021 Maduo

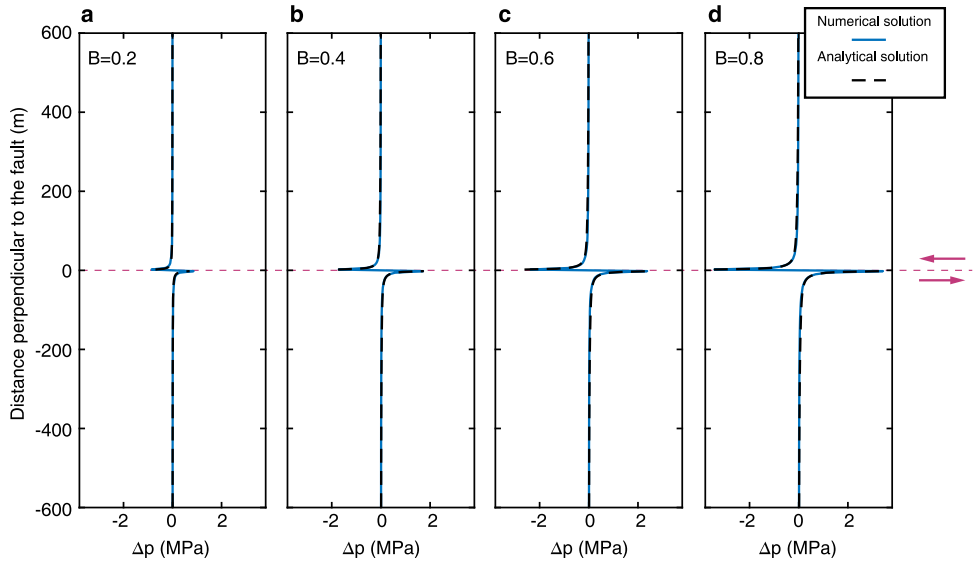

Fig. 8. Comparison between numerical solutions and analytical solutions of static pore pressure change, involving a plane strain shear dislocation within a linear poroelasticity, fluid-saturated solid (Song and Rudnicki, 2017). The purple dashed line indicates the location of the fault plane.

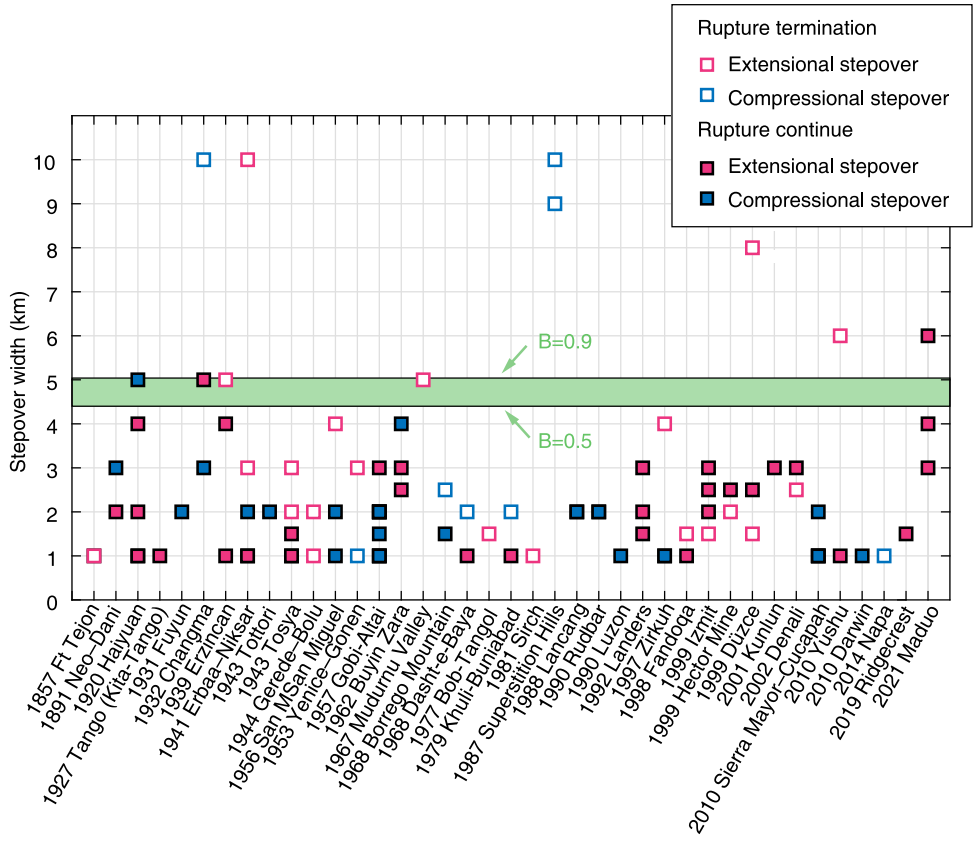

Fig. 9. Observations of stepover width from historical strike-slip earthquake ruptures. The green box indicates the critical stepover width for an equal chance of rupture jumping or arresting, corresponding to Skempton's coefficient ranging from 0.5 to 0.9.

earthquake (Liu et al., 2024). This allowed us to illustrate the stepover widths involved in historical earthquakes and make a meaningful comparison with our simulation results.

Since our 2-D plane simulations specifically focus on the sinistral strike-slip fault setting, we have deliberately excluded dip-slip ruptures from our comparison, as dip-slip ruptures are known to be capable of crossing larger stepovers compared to strike-slip earthquakes, with a maximum distance of approximately 12 km as reported by Biasi and Wesnousky (2016). Consequently, the 2016 Mw 7.8 Kaikōura earthquake, which entailed a complex rupture process involving both thrust and strike-slip faulting (Cesca et al., 2017; Hamling et al., 2017), is not included in our comparison.

Fig. 9 presents a comprehensive comparison of past strike-slip earthquakes, categorizing them based on the maximum stepover width each rupture managed to cross, with a distinction made between compressional and extensional stepovers. Additionally, the figure highlights the

critical stepover widths derived from our numerical simulations, assuming a Skempton's coefficient range of B = 0.5–0.9. This range indicates a 50% chance of rupture propagation across the stepover. The data show a favorable agreement between our simulations and observed field studies; the jumpable widths for compressional stepovers documented in nature consistently remain below our simulated critical stepover width, which is delineated by a green box and spans 4.4 to 5.1 km. Field studies, such as those by Wesnousky (1988) and Knuepfer (1989), confirm that ruptures generally fail to cross compressional stepovers wider than 5 km. This alignment validates our model's predictions in estimating the threshold jumpable width for compressional stepovers in a statistical context. Our simulation-based statistical analysis provides a valuable framework for evaluating jumpable widths and seismic hazards for the stepover systems. In addition to the results presented in Fig. 9, indicating an approximate threshold step size beyond which a rupture has an equal chance of jumping or terminating, Fig. 6 enables us to assess the relative likelihood of rupture scenarios, i.e., pass through or stop, on a fault that includes steps in its mapped trace.

Although our study does not focus extensively on the extensional stepover, we have gained an understanding of the physical mechanism behind the effective normal stress variation induced by pore pressure changes caused by fault slip (Fig. S4). While it is true that earthquakes can rupture through extensional stepovers at a larger perpendicular distance compared to compressional stepovers (e.g., Harris and Day, 1993; Duan and Oglesby, 2006), it is worth noting that certain fault ruptures actually terminate on extremely narrow extensional stepovers, typically ranging from 1 to 2 km, as illustrated in Fig. 9. This intriguing observation could potentially be attributed to the influence of pore fluids. In dynamic rupture simulations involving a dilational stepover, Harris and Day (1993) demonstrated that undrained poroelasticity hinders rupture propagation by elevating effective normal stress. Liu and Duan (2014) found that the critical width for the extensional stepover be reduced to 1000 m after considering the undrained poroelastic effect. Our simulation also reveals that the critical jumpable width is approximately 1500 m for a poroelastic extensional stepover (Fig. S6). Furthermore, Wesnousky (2006) noticed a significant predominance of observed extensional stepovers over compressional stepovers, as further illustrated in Fig. 9. To explain this observation, Liu and Duan (2014) suggested that time-dependent pore pressure influences the behavior of extensional stepovers. Specifically, they noted that a decrease in pore pressure within these stepovers leads to clamping effects. This reduction helps stabilize pre-existing secondary fractures, thereby preserving the integrity of the extensional stepover. As a result, it becomes more difficult for secondary fractures to link the two main fault segments.

5. Conclusions

We performed 2D earthquake sequence simulations incorporating undrained poroelasticity within a compressional stepover. Systematically varying Skempton's coefficient and the stepover width, we investigate the role of the poroelasticity in impacting rupture propagation across the fault step. Furthermore, we provided a physics-based and statistical assessment of the likelihood of rupture jumping the stepover within a fluid-filled porous environment. The key findings can be summarized as follows:

1. The effective normal stress in a compressional stepover relies on the interplay between two factors: compaction-driven normal stress within the rock matrix and undrained pore pressure changes regulated by Skempton's coefficient and average stress variations. Our findings demonstrate that Skempton's coefficient exerts a considerable influence on the effective normal stress, which ultimately governs the clamping or unclamping behavior of the fault, subsequently impacting the propagation of ruptures across the stepover.
2. The merging effects of stepover width and Skempton's coefficient determine the probability of rupture jumping. Skempton's coefficient, which has an approximately linear relationship with the critical jumpable step size, plays a crucial role in controlling seismic hazards for faults situated in stepover systems. A higher Skempton's coefficient can facilitate rupture jumping across fault segments, even for larger stepover distances.
3. A comparison between analytical and numerical solutions provides physics-based predictions on pore pressure change caused by dynamic ruptures. The analytical solutions tied to Skempton's coefficient and dislocation, offering us effective means for enhancing our ability to assess pore pressure change and related seismic hazards near faults situated close to a stepover.
4. The critical jumping width of 4.4 to 5.1 km for a 50% chance of rupture jumping predicted by our model explains the threshold dimension of the strike-slip step, above which ruptures should rarely pass through.

This study highlights the significance of incorporating poroelastic effects on- and off-fault in understanding the dynamic variations of the effective normal stress, which could significantly alter the overall length of fault rupture. In hazard studies, it is essential to take into account Skempton's coefficient, as it is a critical parameter closely associated with the critical jumpable distance between fault segments within a stepover system.

CRediT authorship contribution statement

Luyuan Huang: Writing – review & editing, Writing – original draft, Visualization, Investigation, Formal analysis, Data curation. **Elías Rafn Heimisson:** Writing – review & editing, Visualization, Software, Resources, Methodology. **Luca Dal Zilio:** Writing – review & editing, Writing – original draft, Validation, Supervision, Project administration, Funding acquisition, Conceptualization.

Declaration of competing interest

The authors declare that they have no known competing financial interests or personal relationships that could have appeared to influence the work reported in this paper.

Acknowledgements

Numerical simulations were performed on the ETH Zürich Euler cluster. Luyuan Huang was financially supported by the National Natural Science Foundation of China (No: 42074111, 42174120) and the China Scholarship Council (No: 202004190042). Luca Dal Zilio was supported by the European Research Council (ERC) Synergy Grant "Fault Activation and Earthquake Rupture" (FEAR) (No: 856559), the Earth Observatory of Singapore (EOS), and the Singapore Ministry of Education Tier 3b project "Investigating Volcano and Earthquake Science and Technology (InVEST)" (No: MOE-MOET32021-0002). Elías Rafn Heimisson thanks the Swiss National Science Foundation for partially supporting this research through the Ambizione grant number PZ00P2 208993. The scripts and model outputs used to generate the figures from our numerical simulations can be accessed and reproduced at: https://doi.org/10.21979/N9/AWSZTR.

Appendix A. Supplementary material

Supplementary material related to this article can be found online at https://doi.org/10.1016/j.epsl.2024.119103.

Data availability

Data produced in this study are available.

References

Bai, Kangchen, Ampuero, Jean-Paul, 2017. Effect of seismogenic depth and background stress on physical limits of earthquake rupture across fault step overs. J. Geophys. Res., Solid Earth 122 (12), 10–280. https://doi.org/10.1002/2017JB014848.

Barbot, Sylvain, 2019. Slow-slip, slow earthquakes, period-two cycles, full and partial ruptures, and deterministic chaos in a single asperity fault. Tectonophysics 768, 228171. https://doi.org/10.1016/j.tecto.2019.228171.

Barbot, Sylvain, 2021. A spectral boundary-integral method for quasi-dynamic ruptures of multiple parallel faults. Bull. Seismol. Soc. Am. 111 (3), 1614–1630. https://doi.org/10.1785/0120210004.

Beeler, N.M., Tullis, T.E., Blanpied, M.L., Weeks, J.D., 1996. Frictional behavior of large displacement experimental faults. J. Geophys. Res., Solid Earth 101 (B4), 8697–8715. https://doi.org/10.1029/96JB00411.

Beeler, N.M., Tullis, T.E., Goldsby, D.L., 2008. Constitutive relationships and physical basis of fault strength due to flash heating. J. Geophys. Res., Solid Earth 113 (B1). https://doi.org/10.1029/2007JB004988.

Biasi, Glenn P., Wesnousky, Steven G., 2016. Steps and gaps in ground ruptures: empirical bounds on rupture propagation. Bull. Seismol. Soc. Am. 106 (3), 1110–1124. https://doi.org/10.1785/0120150175.

Cattania, C., 2019. Complex earthquake sequences on simple faults. Geophys. Res. Lett. 46 (17–18), 10384–10393. https://doi.org/10.1029/2019GL083628.

Cesca, Simone, Zhang, Y., Mouslopoulou, V., Wang, R., Saul, Joachim, Savage, M., Heimann, Sebastian, Kufner, S.-K., Oncken, O., Dahm, T., 2017. Complex rupture process of the Mw 7.8, 2016, Kaikoura earthquake, New Zealand, and its aftershock sequence. Earth Planet. Sci. Lett. 478, 110–120. https://doi.org/10.1016/j.epsl.2017.08.024.

Cheng, Alexander H.-D., 2016. Poroelasticity. Springer.

Dal Zilio, Luca, Gerya, Taras, 2022. Subduction earthquake cycles controlled by episodic fluid pressure cycling. Lithos 426, 106800. https://doi.org/10.1016/j.lithos.2022.106800.

Dal Zilio, Luca, Hegyi, Betti, Behr, Whitney, Gerya, Taras, 2022. Hydro-mechanical earthquake cycles in a poro-visco-elasto-plastic fluid-bearing fault structure. Tectonophysics 838, 229516. https://doi.org/10.1016/j.tecto.2022.229516.

Day, Steven M., Dalguer, Luis A., Lapusta, Nadia, Liu, Yi., 2005. Comparison of finite difference and boundary integral solutions to three-dimensional spontaneous rupture. J. Geophys. Res., Solid Earth 110 (B12). https://doi.org/10.1029/2005JB003813.

Dieterich, James H., 1978. Time-dependent friction and the mechanics of stick-slip. Pure Appl. Geophys. 116, 790–806. https://doi.org/10.1007/BF00876539.

Dieterich, James H., 1979. Modeling of rock friction: 1. Experimental results and constitutive equations. J. Geophys. Res., Solid Earth 84 (B5), 2161–2168. https://doi.org/10.1029/JB084iB05p02161.

Dieterich, J.H., 1981. Constitutive Properties of Faults with Simulated Gouge. Monograph 24: Mechanical Behavior of Crustal Rocks. American Geophysical Union, Washington, DC, pp. 103–120.

Duan, Benchun, Oglesby, David D., 2006. Heterogeneous fault stresses from previous earthquakes and the effect on dynamics of parallel strike-slip faults. J. Geophys. Res., Solid Earth 111 (B5). https://doi.org/10.1029/2005JB004138.

Dunham, Eric M., Rice, James R., 2008. Earthquake slip between dissimilar poroelastic materials. J. Geophys. Res., Solid Earth 113 (B9). https://doi.org/10.1029/2007JB005405.

Finzi, Y., Langer, S., 2012. Damage in step-overs may enable large cascading earthquakes. Geophys. Res. Lett. 39 (16). https://doi.org/10.1029/2012GL052436.

Goldberg, Dara E., Melgar, Diego, Sahakian, V.J., Thomas, A.M., Xu, Xiaohua, Crowell, B.W., Geng, J., 2020. Complex rupture of an immature fault zone: a simultaneous kinematic model of the 2019 Ridgecrest, CA earthquakes. Geophys. Res. Lett. 47 (3), e2019GL086382. https://doi.org/10.1029/2019GL086382.

Hamling, Ian J., Hreinsdóttir, Sigrún, Clark, Kate, Elliott, John, Liang, Cunren, Fielding, Eric, Litchfield, Nicola, Villamor, Pilar, Wallace, Laura, Wright, Tim J., et al., 2017. Complex multifault rupture during the 2016 M w 7.8 Kaikōura earthquake, New Zealand. Science 356 (6334), eaam7194. https://doi.org/10.1126/science.aam7194.

Harris, Ruth A., Day, Steven M., 1993. Dynamics of fault interaction: parallel strike-slip faults. J. Geophys. Res., Solid Earth 98 (B3), 4461–4472. https://doi.org/10.1029/92JB02272.

Harris, Ruth A., Simpson, Robert W., 1998. Suppression of large earthquakes by stress shadows: a comparison of Coulomb and rate-and-state failure. J. Geophys. Res., Solid Earth 103 (B10), 24439–24451. https://doi.org/10.1029/98JB00793.

Hart, David J., Wang, Herbert F., 1995. Laboratory measurements of a complete set of poroelastic moduli for Berea sandstone and Indiana limestone. J. Geophys. Res., Solid Earth 100 (B9), 17741–17751. https://doi.org/10.1029/95JB01242.

Heimisson, Elías R., Dunham, Eric M., Almquist, Martin, 2019. Poroelastic effects destabilize mildly rate-strengthening friction to generate stable slow slip pulses. J. Mech. Phys. Solids 130, 262–279. https://doi.org/10.1016/j.jmps.2019.06.007.

Heimisson, Elías Rafn, 2020. Crack to pulse transition and magnitude statistics during earthquake cycles on a self-similar rough fault. Earth Planet. Sci. Lett. 537, 116202. https://doi.org/10.1029/JB081i029p05322.

Heimisson, Elías Rafn, Liu, Shengduo, Lapusta, Nadia, Rudnicki, John, 2022. A spectral boundary-integral method for faults and fractures in a poroelastic solid: simulations of a rate-and-state fault with dilatancy, compaction, and fluid injection. J. Geophys. Res., Solid Earth 127 (9), e2022JB024185. https://doi.org/10.1029/2022JB024185.

Ida, Yoshiaki, 1972. Cohesive force across the tip of a longitudinal-shear crack and Griffith's specific surface energy. J. Geophys. Res. 77 (20), 3796–3805. https://doi.org/10.1029/JB077i020p03796.

Im, Kyungjae, Avouac, Jean-Philippe, 2024. Quake-DFN: a software for simulating sequences of induced earthquakes in a discrete fault network. Bull. Seismol. Soc. Am. 114 (5), 2341–2358. https://doi.org/10.1785/0120230299.

Jaeger, John Conrad, Cook, Neville G.W., Zimmerman, Robert, 2009. Fundamentals of Rock Mechanics. John Wiley & Sons.

Jiang, Junle, Erickson, Brittany A., Lambert, Valère R., Ampuero, Jean-Paul, Ando, Ryosuke, Barbot, Sylvain D., Cattania, Camilla, Zilio, Luca Dal, Duan, Benchun, Dunham, Eric M., et al., 2022. Community-driven code comparisons for three-dimensional dynamic modeling of sequences of earthquakes and aseismic slip. J. Geophys. Res., Solid Earth 127 (3), e2021JB023519. https://doi.org/10.1029/2021JB023519.

Jónsson, Sigurjón, Segall, Paul, Pedersen, Rikke, Björnsson, Grímur, 2003. Post-earthquake ground movements correlated to pore-pressure transients. Nature 424 (6945), 179–183. https://doi.org/10.1038/nature01776.

Knuepfer, P.L.K., 1989. Implications of the characteristics of end-points of historical surface fault ruptures for the nature of fault segmentation. In: Fault Segmentation and Controls of Rupture Initiation and Termination, vol. 89, pp. 193–228.

Kroll, Kayla A., Dieterich, James H., Richards-Dinger, Keith B., Oglesby, David D., 2023. 3-D Simulations of earthquakes rupture jumps: 1. Homogeneous pre-stress conditions. Geophys. J. Int., 395–403. https://doi.org/10.1093/gji/ggad048.

Lanza, F., Chamberlain, C.J., Jacobs, K., Warren-Smith, E., Godfrey, H.J., Kortink, M., Thurber, C.H., Savage, M.K., Townend, John, Roecker, S., et al., 2019. Crustal fault connectivity of the Mw 7.8 2016 Kaikōura earthquake constrained by aftershock relocations. Geophys. Res. Lett. 46 (12), 6487–6496. https://doi.org/10.1029/2019GL082780.

Lapusta, Nadia, Liu, Yi., 2009. Three-dimensional boundary integral modeling of spontaneous earthquake sequences and aseismic slip. J. Geophys. Res., Solid Earth 114 (B9). https://doi.org/10.1029/2008JB005934.

Liu, Xiaoli, Deng, Debeier, Jia, Zhige, Liu-Zeng, Jing, Mo, Xinyu, Huang, Yu, Ruan, Qiaozhe, Liu, Juntao, 2024. Refined coseismic slip model and surface deformation of the 2021 Maduo earthquake: implications for sensitivity of rupture behaviors to geometric complexity. Remote Sens. 16 (4), 713. https://doi.org/10.3390/rs16040713.

Liu, Zaifeng, Duan, Benchun, 2014. Dynamics of parallel strike-slip faults with pore fluid pressure change and off-fault damage. Bull. Seismol. Soc. Am. 104 (2), 780–792. https://doi.org/10.1785/0120130112.

Marone, Chris, 1998. Laboratory-derived friction laws and their application to seismic faulting. Annu. Rev. Earth Planet. Sci. 26 (1), 643–696. https://doi.org/10.1146/annurev.earth.26.1.643.

Mia, Md Shumon, Abdelmeguid, Mohamed, Harris, Ruth A., Elbanna, Ahmed E., 2024. Rupture jumping and seismic complexity in models of earthquake cycles for fault stepovers with off-fault plasticity. Bull. Seismol. Soc. Am. 114 (3), 1466–1480. https://doi.org/10.1785/0120230249.

Nikkhoo, Mehdi, Walter, Thomas R., Lundgren, Paul R., Prats-Iraola, Pau, 2016. Compound dislocation models (CDMs) for volcano deformation analyses. Geophys. J. Int. ggw427. https://doi.org/10.1093/gji/ggw427.

Noda, Hiroyuki, Lapusta, Nadia, 2010. Three-dimensional earthquake sequence simulations with evolving temperature and pore pressure due to shear heating: effect of heterogeneous hydraulic diffusivity. J. Geophys. Res., Solid Earth 115 (B12).

Nurminen, Fiia, Baize, Stéphane, Boncio, Paolo, Blumetti, Anna Maria, Cinti, Francesca R., Civico, Riccardo, Guerrieri, Luca, 2022. SURE 2.0–new release of the worldwide database of surface ruptures for fault displacement hazard analyses. Sci. Data 9 (1), 729. https://doi.org/10.1038/s41597-022-01835-z.

Ozawa, So, Ando, Ryosuke, Dunham, Eric M., 2023. Quantifying the probability of rupture arrest at restraining and releasing bends using earthquake sequence simulations. Earth Planet. Sci. Lett. 617, 118276. https://doi.org/10.1016/j.epsl.2023.118276.

Peng, Zhigang, Gomberg, Joan, 2010. An integrated perspective of the continuum between earthquakes and slow-slip phenomena. Nat. Geosci. 3 (9), 599–607. https://doi.org/10.1038/ngeo940.

Ponti, Daniel J., Blair, James Luke, Rosa, Carla M., Thomas, Kate, Pickering, Alexandra J., Akciz, Sinan, Angster, Stephen, Avouac, Jean-Philipe, Bachhuber, Jeffrey, Bacon, Steven, et al., 2020. Documentation of surface fault rupture and ground-deformation features produced by the 4 and 5 July 2019 Mw 6.4 and Mw 7.1 Ridgecrest earthquake sequence. Seismol. Res. Lett. 91 (5), 2942–2959. https://doi.org/10.1785/0220190322.

Rice, James R., 1993. Spatio-temporal complexity of slip on a fault. J. Geophys. Res., Solid Earth 98 (B6), 9885–9907. https://doi.org/10.1029/93JB00191.

Rice, James R., 2006. Heating and weakening of faults during earthquake slip. J. Geophys. Res., Solid Earth 111 (B5).

Rice, James R., Cleary, Michael P., 1976. Some basic stress diffusion solutions for fluid-saturated elastic porous media with compressible constituents. Rev. Geophys. 14 (2), 227–241. https://doi.org/10.1029/RG014i002p00227.

Rice, James R., Simons, Donald A., 1976. The stabilization of spreading shear faults by coupled deformation-diffusion effects in fluid-infiltrated porous materials. J. Geophys. Res. 81 (29), 5322–5334. https://doi.org/10.1029/JB081i029p05322.

Richards-Dinger, Keith, Dieterich, James H., 2012. RSQSim earthquake simulator. Seismol. Res. Lett. 83 (6), 983–990. https://doi.org/10.1785/0220120105.

Romanet, Pierre, Bhat, Harsha S., Jolivet, Romain, Madariaga, Raúl, 2018. Fast and slow slip events emerge due to fault geometrical complexity. Geophys. Res. Lett. 45 (10), 4809–4819. https://doi.org/10.1029/2018GL077579.

Rubin, Allen M., Ampuero, J-P., 2005. Earthquake nucleation on (aging) rate and state faults. J. Geophys. Res., Solid Earth 110 (B11). https://doi.org/10.1029/2005JB003686.

Rudnicki, John W., Koutsibelas, D.A., 1991. Steady propagation of plane strain shear cracks on an impermeable plane in an elastic diffusive solid. Int. J. Solids Struct. 27 (2), 205–225. https://doi.org/10.1016/0020-7683(91)90229-9.

Rudnicki, John W., Rice, James R., 2006. Effective normal stress alteration due to pore pressure changes induced by dynamic slip propagation on a plane between dissimilar materials. J. Geophys. Res., Solid Earth 111 (B10). https://doi.org/10.1029/2006JB004396.

Ruina, Andy, 1983. Slip instability and state variable friction laws. J. Geophys. Res., Solid Earth 88 (B12), 10359–10370. https://doi.org/10.1029/JB088iB12p10359.

Ryan, Kenny J., Oglesby, David D., 2014. Dynamically modeling fault step overs using various friction laws. J. Geophys. Res., Solid Earth 119 (7), 5814–5829. https://doi.org/10.1002/2014JB011151.

Scholz, C.H., Gupta, Anupma, 2000. Fault interactions and seismic hazard. J. Geodyn. 29 (3–5), 459–467. https://doi.org/10.1016/S0264-3707(99)00040-X.

Segall, Paul, Pollard, D.D., 1980. Mechanics of discontinuous faults. J. Geophys. Res., Solid Earth 85 (B8), 4337–4350. https://doi.org/10.1029/JB085iB08p04337.

Sibson, Richard H., 1985. Stopping of earthquake ruptures at dilational fault jogs. Nature 316 (6025), 248–251. https://doi.org/10.1038/316248a0.

Sieh, Kerry, Jones, Lucile, Hauksson, Egill, Hudnut, Kenneth, Eberhart-Phillips, Donna, Heaton, Thomas, Hough, Susan, Hutton, Kate, Kanamori, Hiroo, Lilje, Anne, et al., 1993. Near-field investigations of the Landers earthquake sequence, April to July 1992. Science 260 (5105), 171–176. https://doi.org/10.1126/science.260.5105.171.

Song, Yongjia, Rudnicki, John W., 2017. Plane-strain shear dislocation on a leaky plane in a poroelastic solid. J. Appl. Mech. 84 (2), 021008. https://doi.org/10.1115/1.4035179.

Stein, Ross S., 1999. The role of stress transfer in earthquake occurrence. Nature 402 (6762), 605–609. https://doi.org/10.1038/45144.

Taufiqurrahman, Taufiq, Gabriel, Alice-Agnes, Li, Duo, Ulrich, Thomas, Li, Bo, Carena, Sara, Verdecchia, Alessandro, Gallovič, František, 2023. Dynamics, interactions and delays of the 2019 Ridgecrest rupture sequence. Nature, 1–8. https://doi.org/10.1038/s41586-023-05985-x.

Thomas, Marion Y., Lapusta, Nadia, Noda, Hiroyuki, Avouac, Jean-Philippe, 2014. Quasi-dynamic versus fully dynamic simulations of earthquakes and aseismic slip with and without enhanced coseismic weakening. J. Geophys. Res., Solid Earth 119 (3), 1986–2004. https://doi.org/10.1002/2013JB010615.

Ulrich, Thomas, Gabriel, Alice-Agnes, Ampuero, Jean-Paul, Xu, Wenbin, 2019. Dynamic viability of the 2016 Mw 7.8 Kaikōura earthquake cascade on weak crustal faults. Nat. Commun. 10 (1), 1213. https://doi.org/10.1038/s41467-019-09125-w.

Wells, Donald L., Coppersmith, Kevin J., 1994. New empirical relationships among magnitude, rupture length, rupture width, rupture area, and surface displacement. Bull. Seismol. Soc. Am. 84 (4), 974–1002. https://doi.org/10.1785/BSSA0840040974.

Wesnousky, Steven G., 1988. Seismological and structural evolution of strike-slip faults. Nature 335 (6188), 340–343. https://doi.org/10.1038/335340a0.

Wesnousky, Steven G., 2006. Predicting the endpoints of earthquake ruptures. Nature 444 (7117), 358–360. https://doi.org/10.1038/nature05275.

Wesnousky, Steven G., 2008. Displacement and geometrical characteristics of earthquake surface ruptures: issues and implications for seismic-hazard analysis and the process of earthquake rupture. Bull. Seismol. Soc. Am. 98 (4), 1609–1632. https://doi.org/10.1785/0120070111.

Yin, Yifan, Galvez, Percy, Heimisson, Elías Rafn, Wiemer, Stefan, 2023. The role of three-dimensional fault interactions in creating complex seismic sequences. Earth Planet. Sci. Lett. 606, 118056. https://doi.org/10.1016/j.epsl.2023.118056.

Zhu, Weiqiang, Allison, Kali L., Dunham, Eric M., Yang, Yuyun, 2020. Fault valving and pore pressure evolution in simulations of earthquake sequences and aseismic slip. Nat. Commun. 11 (1), 4833. https://doi.org/10.1038/s41467-020-18598-z.